

Spherical prism magnetic effects by Gauss–Legendre quadrature integration

M. F. Asgharzadeh,¹ R. R. B. von Frese¹ and H. R. Kim²

¹*School of Earth Sciences, Ohio State University, Columbus, OH, 43210, USA. E-mail: vonfrese@osu.edu*

²*Goddard Earth Sciences & Technology Center, University of Maryland, Baltimore County, GSFC/NASA, Greenbelt, MD, 20771, USA*

Accepted 2007 November 20. Received 2007 November 20; in original form 2007 January 19

SUMMARY

Regional spherical coordinate observations of the Earth's crustal magnetic field components are becoming increasingly available from shipborne, airborne, and satellite surveys. In assessing the geological significance of these data, theoretical anomalous magnetic fields from geologic models in spherical coordinates need to be evaluated. This study explicitly develops the elegant Gauss–Legendre quadrature formulation for numerically modelling the complete magnetic effects (i.e. potential, vector and tensor gradient fields) of the spherical prism. We also use these results to demonstrate the magnetic effects for the crustal prism and to investigate the crustal magnetic effects at satellite altitudes for a large region of the Middle East centred on Iran.

Key words: Magnetic anomalies: modelling and interpretation; Satellite magnetics; Planetary tectonics.

1 INTRODUCTION

The magnetic anomaly fields of large regions of the Earth are being increasingly mapped for geological analysis. Regional airborne and shipborne survey compilations currently exist for North America (Hinze *et al.* 1988; Finn *et al.* 2001), South America (SAMMP) (Pereira & Fuck 2005), the North Atlantic and Arctic (Verhoef *et al.* 1996), the Antarctic south of 60°S (Golynsky *et al.* 2001), Australia (Reeves 2001), Arabia-India-Middle East (AAIME) (Reeves 2003), Europe (Wonik *et al.* 2001) and Africa (AMMP) (Barritt 1993). The International Association of Geomagnetism and Aeronomy (IAGA) has initiated a major project to integrate these regional data sets into a global compilation (Hemant *et al.* 2007). Complementary Ørsted and CHAMP satellite magnetic observations at mean altitudes of roughly 650 and 400 km, respectively, provide additional insights on regional magnetic variations of the lithosphere and important boundary conditions on quantitative geological modelling of the near-surface survey data (e.g. Langel & Hinze 1998).

These regional data sets are registered in the Earth's spherical coordinates and represent a variety of magnetic anomaly components. The airborne and shipborne measurements, for example, include mostly total magnetic field anomalies, as well as vector magnetic observations from the US Navy's Project Magnet surveys. Considerable interest has also developed recently for mapping and interpreting airborne magnetic gradient anomalies (Busby *et al.* 1991) especially for hydrocarbon exploration (Mushayandebu & Davies 2006). Integrating these applications with available regional data sets will require the capability to accurately model the magnetic gradient effects of the regional anomaly data and the underlying terrain.

Satellite magnetic observations, by contrast, are magnetic vector measurements to within the precision of about 0.5 nT (Merayo *et al.* 2000). The Ørsted and CHAMP magnetic missions will be augmented with a constellation of three near polar orbiting satellites that will be launched near the end of the present decade as part of the Swarm mission (ESA 2004). These Swarm magnetic measurements at the altitudes of 450–550 km can be converted into gradient anomalies that will greatly improve crustal anomaly estimates, especially in the polar regions where the distorting effects of the temporally varying external magnetic fields are strongest.

Satellites have also mapped the magnetic fields of the Moon (e.g. Lin *et al.* 1998), Mars (e.g. Arkani-Hamed 2004), and Venus (e.g. Sjogren *et al.* 1997). These magnetic observations are providing critical constraints for modelling the geological properties and evolution of these terrestrial bodies.

To exploit the geological utility of this rapidly growing inventory of regional magnetic data, we must accurately calculate the spherical coordinate magnetic component effects of regionally magnetized bodies. Sharma (1986) gave expressions for the magnetic potential and vector field components of the Cartesian prism. Ku (1977) presented a numerical method based on Gauss–Legendre quadrature (GLQ) integration to calculate the potential and vector field components of the Cartesian prism from the point magnetic dipole effects. The Cartesian expressions are laborious to implement accurately in regional spherical coordinate applications (e.g. von Frese *et al.* 1981a). Thus, von Frese *et al.* (1981a)

adapted the Gauss–Legendre procedure for modelling the spherical coordinate magnetic potential and vector fields of the spherical prism using the spherical point magnetic dipole effects from von Frese *et al.* (1981b) and von Frese (1998).

In this study, we extend the elegant GLQ formulation for modelling the complete magnetic effects (i.e. potential, vector and tensor gradient fields) of the spherical prism. We also use these results to demonstrate the magnetic effects for the crustal prism and to investigate at satellite altitudes the crustal magnetic effects over a large region of the Middle East centred on Iran.

2 OPERATIONAL PRINCIPLES

Magnetic surveys involve spatial measurements of geomagnetic field perturbations \mathbf{B}_0 caused by horizontal variations in the magnetic properties or polarization of the subsurface. In source-free space, the curl of \mathbf{B}_0 (e.g. Langel & Hinze 1998) is:

$$\nabla \times \mathbf{B}_0 = 0, \quad (1)$$

so we can relate \mathbf{B}_0 to the gradient of the scalar potential (P_o) as:

$$\mathbf{B}_0 = \nabla P_o. \quad (2)$$

In the next sections, we develop expressions for the magnetic effects of the point dipole, and then generalize these effects for the arbitrarily shaped macroscopic body made up of point dipoles. We next adapt the generalized effects to the specific analytical expressions of the spherical prism, which in turn we numerically evaluate with least squares accuracy by GLQ integration.

2.1 Point dipole magnetic effects

The point magnetic dipole is defined (e.g. Anderson 1922) as two monopoles of equal strength (dp) (in Am), but of opposite polarities that are separated by the infinitesimally small distance l (in m). In this paper, we assign negative polarity to the north pole and positive polarity to the south pole (Fig. 1). Let the centre of the dipole be at $S(x_s, y_s, z_s)$ in Earth-centred Cartesian coordinates and at $S(r_s, \theta_s, \phi_s)$ in geocentric spherical coordinates with θ -degrees colatitude and ϕ -degrees longitude. Now, at the observation point $O(x_o, y_o, z_o)$ and $O(r_o, \theta_o, \phi_o)$ located at the distance $R_{os} \gg l$, the dipole's scalar magnetic potential to very good approximation is given by:

$$dP_{os} = -\frac{\mu_o}{4\pi} \frac{\cos \alpha}{R_{os}^2} dm_s, \quad (3)$$

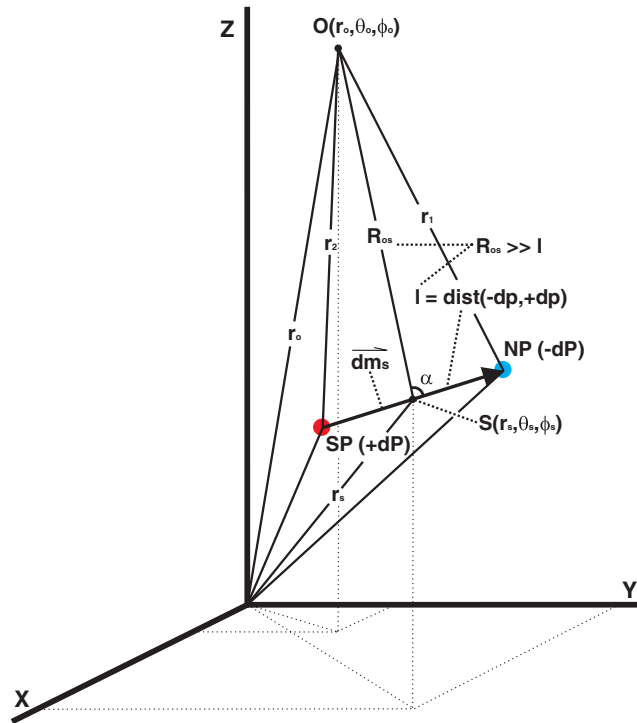


Figure 1. The differential magnetic dipole ($-dP, +dP$) at source point $S(r_s, \theta_s, \phi_s)$ produces a scalar potential dP_{os} at the observation point $O(r_o, \theta_o, \phi_o)$. The magnetic moment vector \mathbf{dm}_s may be represented either by its magnitude dm_s , declination D_s and inclination I_s , or its vector components in the Earth-centred Cartesian ($dm_{s,x}, dm_{s,y}, dm_{s,z}$) or spherical ($dm_{s,r_s}, dm_{s,\theta_s}, dm_{s,\phi_s}$) coordinate systems.

where μ_o is the permeability of air ($= 4\pi \times 10^{-7} \text{ NA}^{-2}$), and

$$\cos \alpha = \frac{dm_{s,x} R_{os,x} + dm_{s,y} R_{os,y} + dm_{s,z} R_{os,z}}{dm_s R_{os}}. \quad (4)$$

The displacement vector \mathbf{R}_{os} connects the centre of the point dipole to the observation point, and the dipole's total magnetic moment vector \mathbf{dm}_s with magnitude $dm_s = l \cdot dp$ (in Am^2) is directed along the dipole's axis from its south to north poles (Fig. 1).

The dipole's total magnetic moment \mathbf{dm}_s is the sum of its induced and remanent moments. Its Cartesian vector components ($dm_{s,x}$, $dm_{s,y}$, $dm_{s,z}$) are related to its spherical vector components (dm_{s,r_s} , dm_{s,θ_s} , dm_{s,ϕ_s}) by:

$$\begin{pmatrix} dm_{s,x} \\ dm_{s,y} \\ dm_{s,z} \end{pmatrix} = \begin{pmatrix} \sin \theta_s \cos \phi_s & \cos \theta_s \cos \phi_s & -\sin \phi_s \\ \sin \theta_s \sin \phi_s & \cos \theta_s \sin \phi_s & \cos \phi_s \\ \cos \theta_s & -\sin \theta_s & 0 \end{pmatrix} \begin{pmatrix} dm_{s,r_s} \\ dm_{s,\theta_s} \\ dm_{s,\phi_s} \end{pmatrix}. \quad (5a)$$

Magnetization is also commonly defined by the intensity (dm_s), declination (D_s) and inclination (I_s) of the source dipole (e.g. von Frese *et al.* 1981b, 1988; von Frese 1998; Blakely 2001), so that we can write eq. (5a) as:

$$\begin{pmatrix} dm_{s,x} \\ dm_{s,y} \\ dm_{s,z} \end{pmatrix} = dm_s \begin{pmatrix} \sin \theta_s \cos \phi_s & \cos \theta_s \cos \phi_s & -\sin \phi_s \\ \sin \theta_s \sin \phi_s & \cos \theta_s \sin \phi_s & \cos \phi_s \\ \cos \theta_s & -\sin \theta_s & 0 \end{pmatrix} \begin{pmatrix} -\sin I_s \\ -\cos I_s \cos D_s \\ \cos I_s \sin D_s \end{pmatrix}. \quad (5b)$$

Additionally, the Cartesian and spherical components of the displacement vector \mathbf{R}_{os} are related by:

$$\begin{pmatrix} R_{os,x} \\ R_{os,y} \\ R_{os,z} \end{pmatrix} = \begin{pmatrix} r_{o,x} \\ r_{o,y} \\ r_{o,z} \end{pmatrix} - \begin{pmatrix} r_{s,x} \\ r_{s,y} \\ r_{s,z} \end{pmatrix} = \begin{pmatrix} r_o \sin \theta_o \cos \phi_o \\ r_o \sin \theta_o \sin \phi_o \\ r_o \cos \theta_o \end{pmatrix} - \begin{pmatrix} r_s \sin \theta_s \cos \phi_s \\ r_s \sin \theta_s \sin \phi_s \\ r_s \cos \theta_s \end{pmatrix}. \quad (6)$$

Thus, the vector components of the magnetic field of the dipole (\mathbf{dB}_{os}) may be obtained by:

$$\nabla(dP_{os}) = \mathbf{dB}_{os}, \quad (7)$$

with the higher order spatial gradients calculated from:

$$\nabla(\mathbf{dB}_{os}). \quad (8)$$

2.2 Generalized magnetic effects for an extended body

The equations in the previous section are for the magnetic effects of the point dipole only, whereas in geophysical practice the operative physical property is the magnetic moment per volume dV (in m^3) of the source or its magnetization $\mathbf{M}_s = \mathbf{dm}_s/dV$ (in A m^{-1}). Taking magnetization into account, the point dipole's magnetic effects in eqs (3), (4), (5a), (5b), (7) and (8), respectively, become:

$$dP_{os} = -\frac{\mu_o}{4\pi} \left(\frac{\cos \alpha}{R_{os}^2} \right) (M_s dV), \quad (9)$$

$$\cos \alpha = \frac{M_{s,x} R_{os,x} + M_{s,y} R_{os,y} + M_{s,z} R_{os,z}}{M_s R_{os}}, \quad (10)$$

$$\begin{pmatrix} M_{s,x} \\ M_{s,y} \\ M_{s,z} \end{pmatrix} = \begin{pmatrix} \sin \theta_s \cos \phi_s & \cos \theta_s \cos \phi_s & -\sin \phi_s \\ \sin \theta_s \sin \phi_s & \cos \theta_s \sin \phi_s & \cos \phi_s \\ \cos \theta_s & -\sin \theta_s & 0 \end{pmatrix} \begin{pmatrix} M_{s,r_s} \\ M_{s,\theta_s} \\ M_{s,\phi_s} \end{pmatrix}, \quad (11a)$$

$$\begin{pmatrix} M_{s,x} \\ M_{s,y} \\ M_{s,z} \end{pmatrix} = M_s \begin{pmatrix} \sin \theta_s \cos \phi_s & \cos \theta_s \cos \phi_s & -\sin \phi_s \\ \sin \theta_s \sin \phi_s & \cos \theta_s \sin \phi_s & \cos \phi_s \\ \cos \theta_s & -\sin \theta_s & 0 \end{pmatrix} \begin{pmatrix} -\sin I_s \\ -\cos I_s \cos D_s \\ \cos I_s \sin D_s \end{pmatrix}, \quad (11b)$$

$$\mathbf{dB}_{os} = -\frac{\mu_o}{4\pi} \left[\nabla \left(\frac{\cos \alpha}{R_{os}^2} \right) \right] (M_s dV) \quad (12)$$

and

$$\nabla(\mathbf{dB}_{os}) = -\frac{\mu_o}{4\pi} \left\{ \nabla \left[\nabla \left(\frac{\cos \alpha}{R_{os}^2} \right) \right] \right\} (M_s dV), \quad (13)$$



Table 3. Formula for dB_{os,ϕ_o} in eq. (22c).

$dB_{os,\phi_o} = k \frac{N_3}{D_3} dr_s d\theta_s d\phi_s$
$N_3 = A_3 R_{os}^2 - 3 r_s \sin \theta_s B_3 C_3$
$A_3 = -M_{s,x} \sin \phi_o + M_{s,y} \cos \phi_o$
$B_3 = \sin(\phi_o - \phi_s)$
$C_3 = M_{s,x} R_{os,x} + M_{s,y} R_{os,y} + M_{s,z} R_{os,z}$
$D_3 = R_{os}^3$

Table 4. Formulae for the tensor gradient elements of Matrix 23.

Component	Formula
dB_{os,r_o,r_o}	$\frac{\partial(dB_{os,r_o})}{\partial r_o}$
dB_{os,r_o,θ_o}	$\frac{1}{r_o} \left(\frac{\partial(dB_{os,r_o})}{\partial \theta_o} - dB_{os,\theta_o} \right)$
dB_{os,r_o,ϕ_o}	$\frac{1}{r_o \sin \theta_o} \left(\frac{\partial(dB_{os,r_o})}{\partial \phi_o} - dB_{os,\phi_o} \sin \theta_o \right)$
dB_{os,θ_o,r_o}	$\frac{\partial(dB_{os,\theta_o})}{\partial r_o}$
$dB_{os,\theta_o,\theta_o}$	$\frac{1}{r_o} \left(\frac{\partial(dB_{os,\theta_o})}{\partial \theta_o} + dB_{os,r_o} \right)$
dB_{os,θ_o,ϕ_o}	$\frac{1}{r_o \sin \theta_o} \left(\frac{\partial(dB_{os,\theta_o})}{\partial \phi_o} - dB_{os,\phi_o} \cos \theta_o \right)$
dB_{os,ϕ_o,r_o}	$\frac{\partial(dB_{os,\phi_o})}{\partial r_o}$
dB_{os,ϕ_o,θ_o}	$\frac{1}{r_o} \frac{\partial(dB_{os,\phi_o})}{\partial \theta_o}$
dB_{os,ϕ_o,ϕ_o}	$\frac{1}{r_o \sin \theta_o} \frac{\partial(dB_{os,\phi_o})}{\partial \phi_o} + \frac{1}{r_o} dB_{os,r_o} + \frac{\cot \theta_o}{r_o} dB_{os,\theta_o}$

$$\mathbf{B}_o = \int_V d\mathbf{B}_{os} = -\frac{\mu_o}{4\pi} \int_V \left[\nabla \left(\frac{\cos \alpha}{R_{os}^2} \right) \right] M_s dV \quad (15)$$

and

$$\nabla(\mathbf{B}_o) = \int_V \nabla(d\mathbf{B}_{os}) = -\frac{\mu_o}{4\pi} \int_V \left\{ \nabla \left[\nabla \left(\frac{\cos \alpha}{R_{os}^2} \right) \right] \right\} M_s dV. \quad (16)$$

Note that after representing dV in an appropriate spatial coordinate system, each of the integrands of eqs (14)–(16) can be generalized according to the relation:

$$q \left(\frac{\cos \alpha}{R_{os}^2} \right) \Delta X, \quad (17)$$

where ΔX is strictly a function of the source parameters and $q(\frac{\cos \alpha}{R_{os}^2})$ is a function of the displacement geometry. For example, in modelling the potential, the geometric function is $(\frac{\cos \alpha}{R_{os}^2})$, whereas for modelling the magnetic field it becomes $\nabla(\frac{\cos \alpha}{R_{os}^2})$, and so forth.

Table 5. Partial differentials of R_{os} (eq. 18) in the respective r_o -, θ_o - and ϕ_o -direction for calculating the tensor gradient components in Tables 6–14 with $\cos \delta$ defined as in eq. (19).

$R'_{os,r_o} = \frac{r_o - r_s \cos \delta}{R_{os}}$
$R'_{os,\theta_o} = \frac{r_o r_s}{R_{os}} [\sin \theta_o \cos \theta_s - \cos \theta_o \sin \theta_s \cos(\phi_o - \phi_s)]$
$R'_{os,\phi_o} = \frac{r_o r_s}{R_{os}} \sin \theta_o \sin \theta_s \sin(\phi_o - \phi_s)$

Table 6. Formula for $\frac{\partial}{\partial r_o}(dB_{os,r_o})$ in Table 4.

$\frac{\partial}{\partial r_o}(dB_{os,r_o}) = k \frac{N'_{1,r_o} D_1 - D'_{1,r_o} N_1}{D_1^2} dr_s d\theta_s d\phi_s$
$N'_{1,r_o} = A'_{1,r_o} R_{os}^2 + 2R'_{os,r_o} R_{os} A_1 - 3B'_{1,r_o} C_1 - 3B_1 C'_{1,r_o}$
$A'_{1,r_o} = 0$
$B'_{1,r_o} = 1$
$C'_{1,r_o} = M_{s,x} \sin \theta_o \cos \phi_o + M_{s,y} \sin \theta_o \sin \phi_o + M_{s,z} \cos \theta_o$
$D'_{1,r_o} = 5R_{os}^3(r_o - r_s \cos \delta)$

Table 7. Formula for $\frac{\partial}{\partial \theta_o}(\mathrm{d}B_{os,r_o})$ in Table 4.

$\frac{\partial}{\partial \theta_o}(\mathrm{d}B_{os,r_o}) = k \frac{N'_{1,\theta_o} D_1 - D'_{1,\theta_o} N_1}{D_1^2} \mathrm{d}r_s \mathrm{d}\theta_s \mathrm{d}\phi_s$
$N'_{1,\theta_o} = A'_{1,\theta_o} R_{os}^2 + 2R'_{os,\theta_o} R_{os} A_1 - 3B'_{1,\theta_o} C_1 - 3B_1 C'_{1,\theta_o}$
$A'_{1,\theta_o} = M_{s,x} \cos \theta_o \cos \phi_o + M_{s,y} \cos \theta_o \sin \phi_o - M_{s,z} \sin \theta_o$
$B'_{1,\theta_o} = r_s [\sin \theta_o \cos \theta_s - \cos \theta_o \sin \theta_s \cos(\phi_o - \phi_s)]$
$C'_{1,\theta_o} = M_{s,x} r_o \cos \theta_o \cos \phi_o + M_{s,y} r_o \cos \theta_o \sin \phi_o - M_{s,z} r_o \sin \theta_o$
$D'_{1,\theta_o} = 5r_o r_s R_{os}^3 [\sin \theta_o \cos \theta_s - \cos \theta_o \sin \theta_s \cos(\phi_o - \phi_s)]$

Table 8. Formula for $\frac{\partial}{\partial \phi_o}(\mathrm{d}B_{os,r_o})$ in Table 4.

$\frac{\partial}{\partial \phi_o}(\mathrm{d}B_{os,r_o}) = k \frac{N'_{1,\phi_o} D_1 - D'_{1,\phi_o} N_1}{D_1^2} \mathrm{d}r_s \mathrm{d}\theta_s \mathrm{d}\phi_s$
$N'_{1,\phi_o} = A'_{1,\phi_o} R_{os}^2 + 2R'_{os,\phi_o} R_{os} A_1 - 3B'_{1,\phi_o} C_1 - 3B_1 C'_{1,\phi_o}$
$A'_{1,\phi_o} = -M_{s,x} \sin \theta_o \sin \phi_o + M_{s,y} \sin \theta_o \cos \phi_o$
$B'_{1,\phi_o} = r_s \sin \theta_o \sin \theta_s \sin(\phi_o - \phi_s)$
$C'_{1,\phi_o} = -M_{s,x} r_o \sin \theta_o \sin \phi_o + M_{s,y} r_o \sin \theta_o \cos \phi_o$
$D'_{1,\phi_o} = 5r_o r_s R_{os}^3 \sin \theta_o \sin \theta_s \sin(\phi_o - \phi_s)$

2.3 Magnetic effects for the spherical prism

We now adapt the above generalized magnetic modelling results to the specific geometric parameters of the spherical prism (Fig. 2). In particular, we need to account for the spherical coordinate details of the displacement distance R_{os} given by:

$$R_{os} = (r_o^2 + r_s^2 - 2r_o r_s \cos \delta)^{\frac{1}{2}}, \quad (18)$$

where

$$\cos \delta = \cos \theta_o \cos \theta_s + \sin \theta_o \sin \theta_s \cos(\phi_o - \phi_s), \quad (19)$$

and θ_o and θ_s are the colatitude coordinates of the observation and source points, respectively, and ϕ_o and ϕ_s are the respective longitude coordinates. The generalized results must also account for the volume $\mathrm{d}V$ of the spherical prism given by:

$$\mathrm{d}V = r_s^2 \sin \theta_s \mathrm{d}r_s \mathrm{d}\theta_s \mathrm{d}\phi_s. \quad (20)$$

Thus, substituting the above details into eq. (14) obtains the magnetic potential of the spherical prism as:

$$P_o = M_s \int_{\phi_s=\phi_1}^{\phi_2} \int_{\theta_s=\theta_1}^{\theta_2} \int_{r_s=r_1}^{r_2} \frac{k \cos \alpha}{R_{os}^2} \mathrm{d}r_s \mathrm{d}\theta_s \mathrm{d}\phi_s, \quad (21)$$

where $k = -\frac{\mu_o}{4\pi} r_s^2 \sin \theta_s$, and $\cos \alpha$ is defined in eq. (10).

Table 9. Formula for $\frac{\partial}{\partial r_o}(\mathrm{d}B_{os,\theta_o})$ in Table 4.

$\frac{\partial}{\partial r_o}(\mathrm{d}B_{os,\theta_o}) = k \frac{N'_{2,r_o} D_2 - D'_{2,r_o} N_2}{D_2^2} \mathrm{d}r_s \mathrm{d}\theta_s \mathrm{d}\phi_s$
$N'_{2,r_o} = A'_{2,r_o} R_{os}^2 + 2R'_{os,r_o} R_{os} A_2 - 3r_s B'_{2,r_o} C_2 - 3r_s B_2 C'_{2,r_o}$
$A'_{2,r_o} = 0$
$B'_{2,r_o} = 0$
$C'_{2,r_o} = M_{s,x} \sin \theta_o \cos \phi_o + M_{s,y} \sin \theta_o \sin \phi_o + M_{s,z} \cos \theta_o$
$D'_{2,r_o} = 5R_{os}^3 (r_o - r_s \cos \delta)$

Table 10. Formula for $\frac{\partial}{\partial \theta_o}(\mathrm{d}B_{os,\theta_o})$ in Table 4.

$\frac{\partial}{\partial \theta_o}(\mathrm{d}B_{os,\theta_o}) = k \frac{N'_{2,\theta_o} D_2 - D'_{2,\theta_o} N_2}{D_2^2} \mathrm{d}r_s \mathrm{d}\theta_s \mathrm{d}\phi_s$
$N'_{2,\theta_o} = A'_{2,\theta_o} R_{os}^2 + 2R'_{os,\theta_o} R_{os} A_2 - 3r_s B'_{2,\theta_o} C_2 - 3r_s B_2 C'_{2,\theta_o}$
$A'_{2,\theta_o} = -M_{s,x} \sin \theta_o \cos \phi_o - M_{s,y} \sin \theta_o \sin \phi_o - M_{s,z} \cos \theta_o$
$B'_{2,\theta_o} = \cos \theta_o \cos \theta_s + \sin \theta_o \sin \theta_s \cos(\phi_o - \phi_s)$
$C'_{2,\theta_o} = M_{s,x} r_o \cos \theta_o \cos \phi_o + M_{s,y} r_o \cos \theta_o \sin \phi_o - M_{s,z} r_o \sin \theta_o$
$D'_{2,\theta_o} = 5r_o r_s R_{os}^3 [\sin \theta_o \cos \theta_s - \cos \theta_o \sin \theta_s \cos(\phi_o - \phi_s)]$

Table 11. Formula for $\frac{\partial}{\partial \phi_o}(dB_{os,\theta_o})$ in Table 4.

$$\begin{aligned} \frac{\partial}{\partial \phi_o}(dB_{os,\theta_o}) &= k \frac{N'_{2,\phi_o} D_2 - D'_{2,\phi_o} N_2}{D_2^2} dr_s d\theta_s d\phi_s \\ N'_{2,\phi_o} &= A'_{2,\phi_o} R_{os}^2 + 2R'_{os,\phi_o} R_{os} A_2 - 3r_s B'_{2,\phi_o} C_2 - 3r_s B_2 C'_{2,\phi_o} \\ A'_{2,\phi_o} &= -M_{s,x} \cos \theta_o \sin \phi_o + M_{s,y} \cos \theta_o \cos \phi_o \\ B'_{2,\phi_o} &= \cos \theta_o \sin \theta_s \sin(\phi_o - \phi_s) \\ C'_{2,\phi_o} &= -M_{s,x} r_o \sin \theta_o \sin \phi_o + M_{s,y} r_o \sin \theta_o \cos \phi_o \\ D'_{2,\phi_o} &= 5r_o r_s R_{os}^3 \sin \theta_o \sin \theta_s \sin(\phi_o - \phi_s) \end{aligned}$$

Table 12. Formula for $\frac{\partial}{\partial r_o}(dB_{os,\phi_o})$ in Table 4.

$$\begin{aligned} \frac{\partial}{\partial r_o}(dB_{os,\phi_o}) &= k \frac{N'_{3,r_o} D_3 - D'_{3,r_o} N_3}{D_3^2} dr_s d\theta_s d\phi_s \\ N'_{3,r_o} &= A'_{3,r_o} R_{os}^2 + 2R'_{os,r_o} R_{os} A_3 - 3r_s \sin \theta_s B'_{3,r_o} C_3 - 3r_s \sin \theta_s B_3 C'_{3,r_o} \\ A'_{3,r_o} &= 0 \\ B'_{3,r_o} &= 0 \\ C'_{3,r_o} &= M_{s,x} \sin \theta_o \cos \phi_o + M_{s,y} \sin \theta_o \sin \phi_o + M_{s,z} \cos \theta_o \\ D'_{3,r_o} &= 5R_{os}^3 (r_o - r_s \cos \delta) \end{aligned}$$

Similarly, for modelling the magnitudes of the magnetic field vector components, we substitute the spherical coordinate details into eq. (15) to obtain:

$$B_{o,r_o} = \int_{\phi_s=\phi_1}^{\phi_2} \int_{\theta_s=\theta_1}^{\theta_2} \int_{r_s=r_1}^{r_2} dB_{os,r_o}, \quad (22a)$$

$$B_{o,\theta_o} = \int_{\phi_s=\phi_1}^{\phi_2} \int_{\theta_s=\theta_1}^{\theta_2} \int_{r_s=r_1}^{r_2} dB_{os,\theta_o} \quad (22b)$$

and

$$B_{o,\phi_o} = \int_{\phi_s=\phi_1}^{\phi_2} \int_{\theta_s=\theta_1}^{\theta_2} \int_{r_s=r_1}^{r_2} dB_{os,\phi_o}, \quad (22c)$$

where the complete expressions for dB_{o,r_o} , dB_{o,θ_o} and dB_{o,ϕ_o} are presented in Tables 1–3.

For modelling the gradient of the prism's magnetic field, the spherical coordinate details must be incorporated into the gradient components of eq. (16) that are the elements of the 3×3 matrix:

$$\nabla \mathbf{dB}_{os} = \begin{pmatrix} dB_{os,r_o,r_o} & dB_{os,r_o,\theta_o} & dB_{os,r_o,\phi_o} \\ dB_{os,\theta_o,r_o} & dB_{os,\theta_o,\theta_o} & dB_{os,\theta_o,\phi_o} \\ dB_{os,\phi_o,r_o} & dB_{os,\phi_o,\theta_o} & dB_{os,\phi_o,\phi_o} \end{pmatrix}, \quad (23)$$

Table 13. Formula for $\frac{\partial}{\partial \theta_o}(dB_{os,\phi_o})$ in Table 4.

$$\begin{aligned} \frac{\partial}{\partial \theta_o}(dB_{os,\phi_o}) &= k \frac{N'_{3,\theta_o} D_3 - D'_{3,\theta_o} N_3}{D_3^2} dr_s d\theta_s d\phi_s \\ N'_{3,\theta_o} &= A'_{3,\theta_o} R_{os}^2 + 2R'_{os,\theta_o} R_{os} A_3 - 3r_s \sin \theta_s B'_{3,\theta_o} C_3 - 3r_s \sin \theta_s B_3 C'_{3,\theta_o} \\ A'_{3,\theta_o} &= 0 \\ B'_{3,\theta_o} &= 0 \\ C'_{3,\theta_o} &= M_{s,x} r_o \cos \theta_o \cos \phi_o + M_{s,y} r_o \cos \theta_o \sin \phi_o - M_{s,z} r_o \sin \theta_o \\ D'_{3,\theta_o} &= 5r_o r_s R_{os}^3 [\sin \theta_o \cos \theta_s - \cos \theta_o \sin \theta_s \cos(\phi_o - \phi_s)] \end{aligned}$$

Table 14. Formula for $\frac{\partial}{\partial \phi_o}(dB_{os,\phi_o})$ in Table 4.

$$\begin{aligned} \frac{\partial}{\partial \phi_o}(dB_{os,\phi_o}) &= k \frac{N'_{3,\phi_o} D_3 - D'_{3,\phi_o} N_3}{D_3^2} dr_s d\theta_s d\phi_s \\ N'_{3,\phi_o} &= A'_{3,\phi_o} R_{os}^2 + 2R'_{os,\phi_o} R_{os} A_3 - 3r_s \sin \theta_s B'_{3,\phi_o} C_3 - 3r_s \sin \theta_s B_3 C'_{3,\phi_o} \\ A'_{3,\phi_o} &= -M_{s,x} \cos \phi_o - M_{s,y} \sin \phi_o \\ B'_{3,\phi_o} &= \cos(\phi_o - \phi_s) \\ C'_{3,\phi_o} &= -M_{s,x} r_o \sin \theta_o \sin \phi_o + M_{s,y} r_o \sin \theta_o \cos \phi_o \\ D'_{3,\phi_o} &= 5r_o r_s R_{os}^3 \sin \theta_o \sin \theta_s \sin(\phi_o - \phi_s) \end{aligned}$$

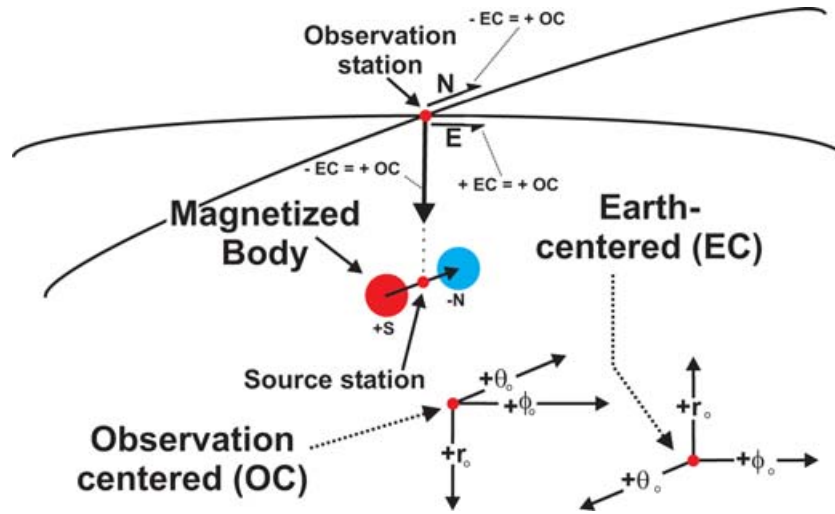


Figure 3. Comparison of the Earth-centred (EC) and Observation-centred (OC) spherical coordinate conventions used in this study. The top diagram compares the conventions for interpreting the magnetic vector and tensor gradient components.

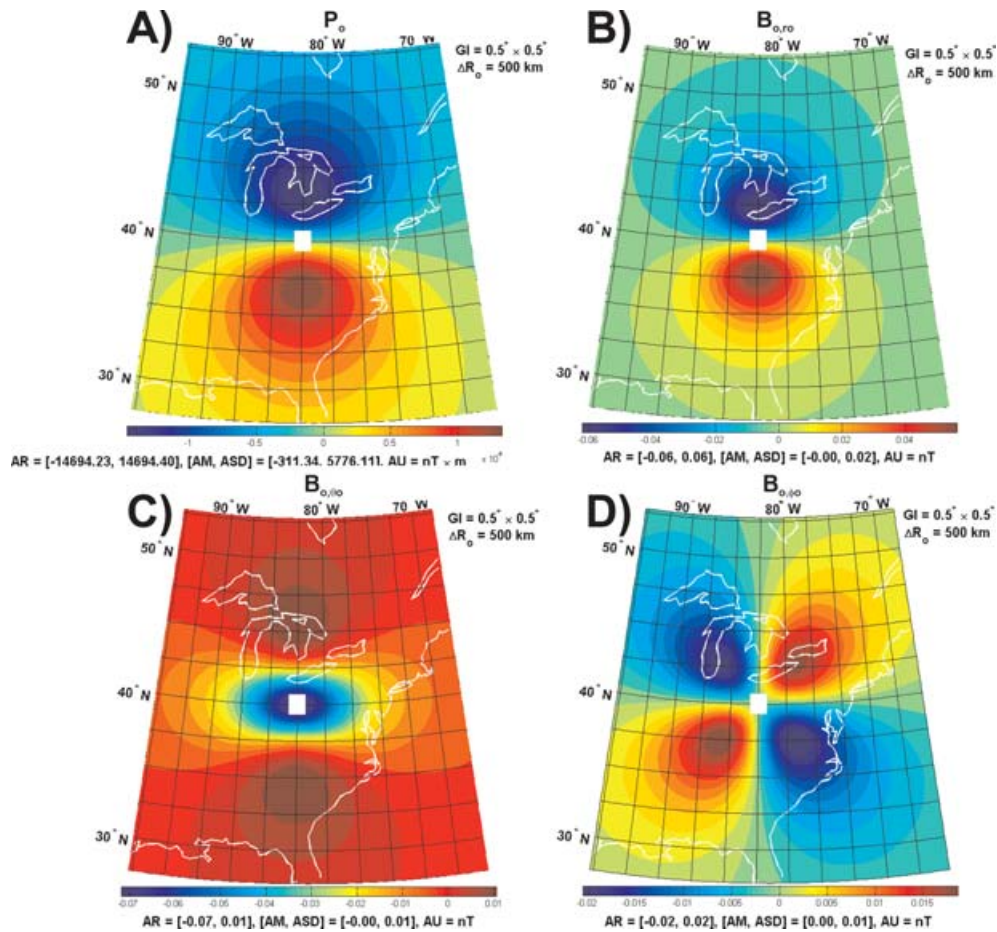


Figure 4. Maps A–D give the respective magnetic potential (P_o) and magnetic radial (B_{o,r_o}), north–south (B_{o,θ_o}) and east–west (B_{o,ϕ_o}) vector anomaly components in the Observation-centred coordinates from the GLQ integration of a $1^\circ \times 1^\circ \times 10$ km prism with 1 Am^{-1} magnetization intensity and $D_s = I_s = 0^\circ$. The magnetic effects were modelled at $\Delta R_o = 500$ km for the spherical prism with its top surface at sea level using $(I = 2) \times (J = 8) \times (K = 8)$ nodes. Map attributes listed in this and subsequent figures include: AM (amplitude mean), AR (amplitude range), ASD (amplitude standard deviation), AU (amplitude unit) and GI (grid interval).

where Table 4 presents the gradient components in detail with the related partial differentials listed in Tables 5–14. Thus, integrating at the observation point the gradient components over the source volume obtains the magnetic tensor gradient components:

$$\mathbf{B}_{0,m,u} = \int_{\phi_s=\phi_1}^{\phi_2} \int_{\theta_s=\theta_1}^{\theta_2} \int_{r_s=r_1}^{r_2} d\mathbf{B}_{0s,m,u}, \quad (24)$$

where m is the r_o -, θ_o -, or ϕ_o -component of (B_o, dB_{os}) and u is the r_o -, θ_o - or ϕ_o -direction along which the gradient is taken.

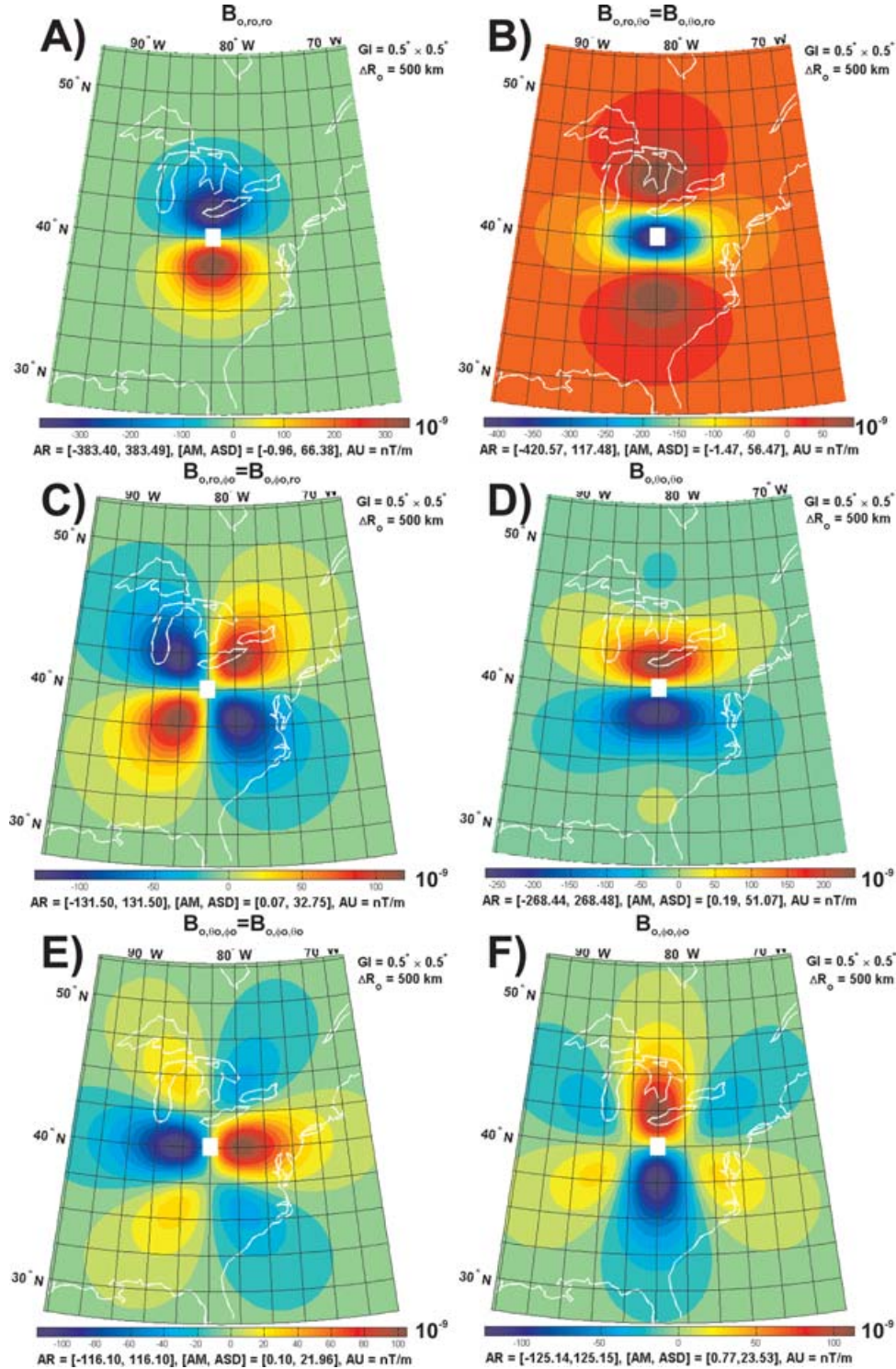


Figure 5. Magnetic tensor gradient components in the Observation-centred coordinates for the spherical prism in Fig. 4. The maps show the 5 unique components of matrix 23 since the three off-diagonal elements are symmetric and Laplace's Equation relates any two of the trace elements to the third one.

Analytically integrating eqs (21), (22) and (24) clearly poses complicated and daunting challenges. Integrating these Equations numerically, on the other hand, is comparatively straightforward because the integrands are analytical functions. Specifically, we can express each of these integrals as the generalized triple integral:

$$\int_{\phi_s=\phi_1}^{\phi_2} \int_{\theta_s=\theta_1}^{\theta_2} \int_{r_s=r_1}^{r_2} f(r_o, \theta_o, \phi_o, r_s, \theta_s, \phi_s) dr_s d\theta_s d\phi_s, \quad (25)$$

which by its GLQ decomposition (Stroud & Secrest 1966; von Frese *et al.* 1981a) has the least squares numerical solution:

$$\frac{(r_2 - r_1)(\theta_2 - \theta_1)(\phi_2 - \phi_1)}{8} \sum_{nk=1}^K \sum_{nj=1}^J \sum_{ni=1}^I A_{ni} A_{nj} A_{nk} f(r_o, \theta_o, \phi_o, \hat{r}_{ni}, \hat{\theta}_{nj}, \hat{\phi}_{nk}). \quad (26)$$

Here, the Gauss–Legendre coefficients (A_{ni} , A_{nj} , A_{nk}) are functions of the coordinates (r_{ni} , θ_{nj} , ϕ_{nk}) of the n th Gaussian node in the interval $(-1, 1)$. Each node is the coordinate for a zero of the n th order Legendre polynomial that orthogonally spans the unit interval. Stroud & Secrest (1966) list the Gaussian coefficients (or weights) and corresponding unit interval coordinates (or nodes) to 30 significant figures for Legendre polynomials of orders $n = 2$ –512. In application (e.g. eq. 25), however, the nodes must be scaled to the actual coordinates (\hat{r}_{ni} , $\hat{\theta}_{nj}$, $\hat{\phi}_{nk}$) within the body by:

$$\hat{r}_{ni} = \frac{r_{ni}(r_2 - r_1) + (r_2 + r_1)}{2}, \quad (27a)$$

$$\hat{\theta}_{nj} = \frac{\theta_{nj}(\theta_2 - \theta_1) + (\theta_2 + \theta_1)}{2} \quad (27b)$$

and

$$\hat{\phi}_{nk} = \frac{\phi_{nk}(\phi_2 - \phi_1) + (\phi_2 + \phi_1)}{2}. \quad (27c)$$

The quadrature formula in eq. (26) shows that the magnetic components of the spherical prism in eqs (21), (22) and (24) can be computed accurately by summing at each observation point the effects of $I \times J \times K$ equivalent point dipoles, where each point dipole located within the prism at the source point coordinate (\hat{r}_{ni} , $\hat{\theta}_{nj}$, $\hat{\phi}_{nk}$) has an effect weighted by the relevant GLQ coefficients and the (r_s, θ_s, ϕ_s) -limits of

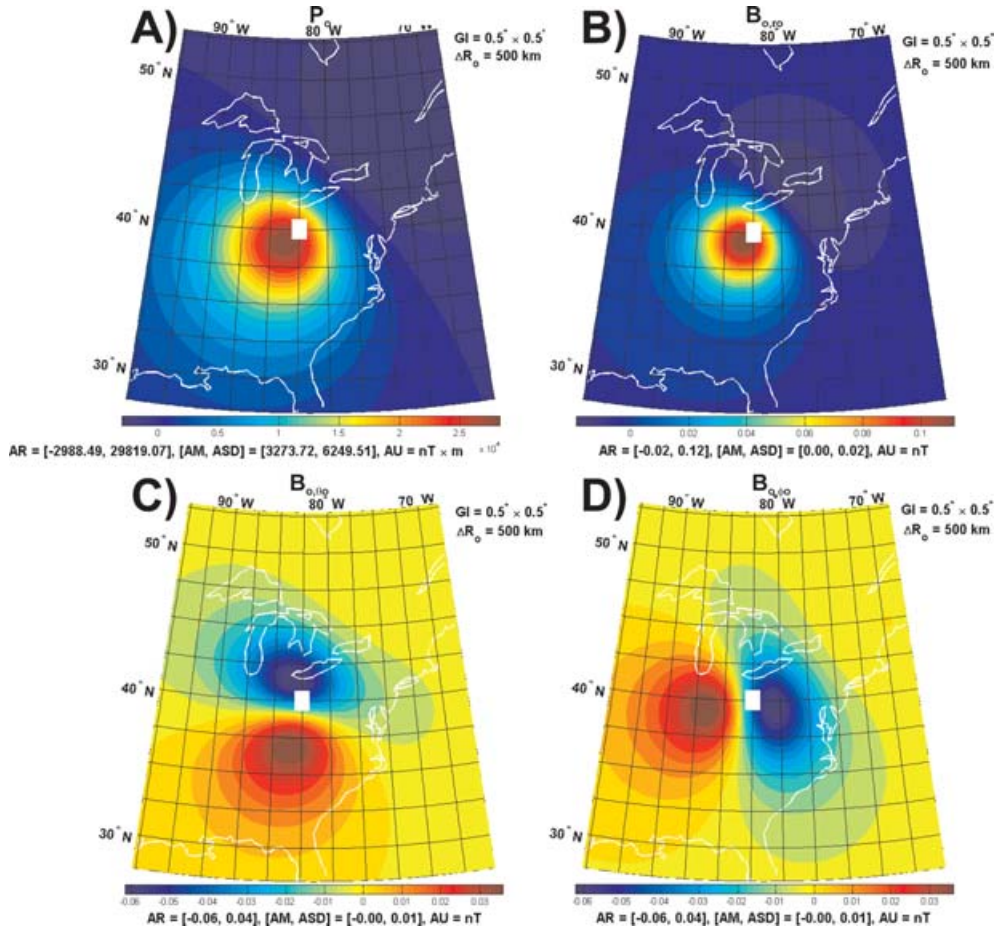


Figure 6. Maps A–D give the respective magnetic potential (P_o) and magnetic radial (B_{o,r_o}), north–south (B_{o,θ_o}) and east–west (B_{o,ϕ_o}) vector anomaly components in the Observation-centred coordinate system for the spherical prism in Fig. 4 with $D_s = I_s = 45^\circ$.

the prism. The only issue remaining in applying eq. (26) is selecting the number of nodes (I, J, K) for the efficient computation of accurate results. A large number of nodes ensures a very accurate quadrature solution, but the highest level of accuracy possible in practice often can be achieved with a substantially smaller number of point sources. Indeed, the accuracy of the solution remains essentially unchanged for different numbers of nodes as long as the node spacing is smaller than the distance to the observation point (Ku 1977; von Frese *et al.* 1981a). Hence, the minimum number of nodes for a given application should be such that the distance to the observation point is greater than the node spacing.

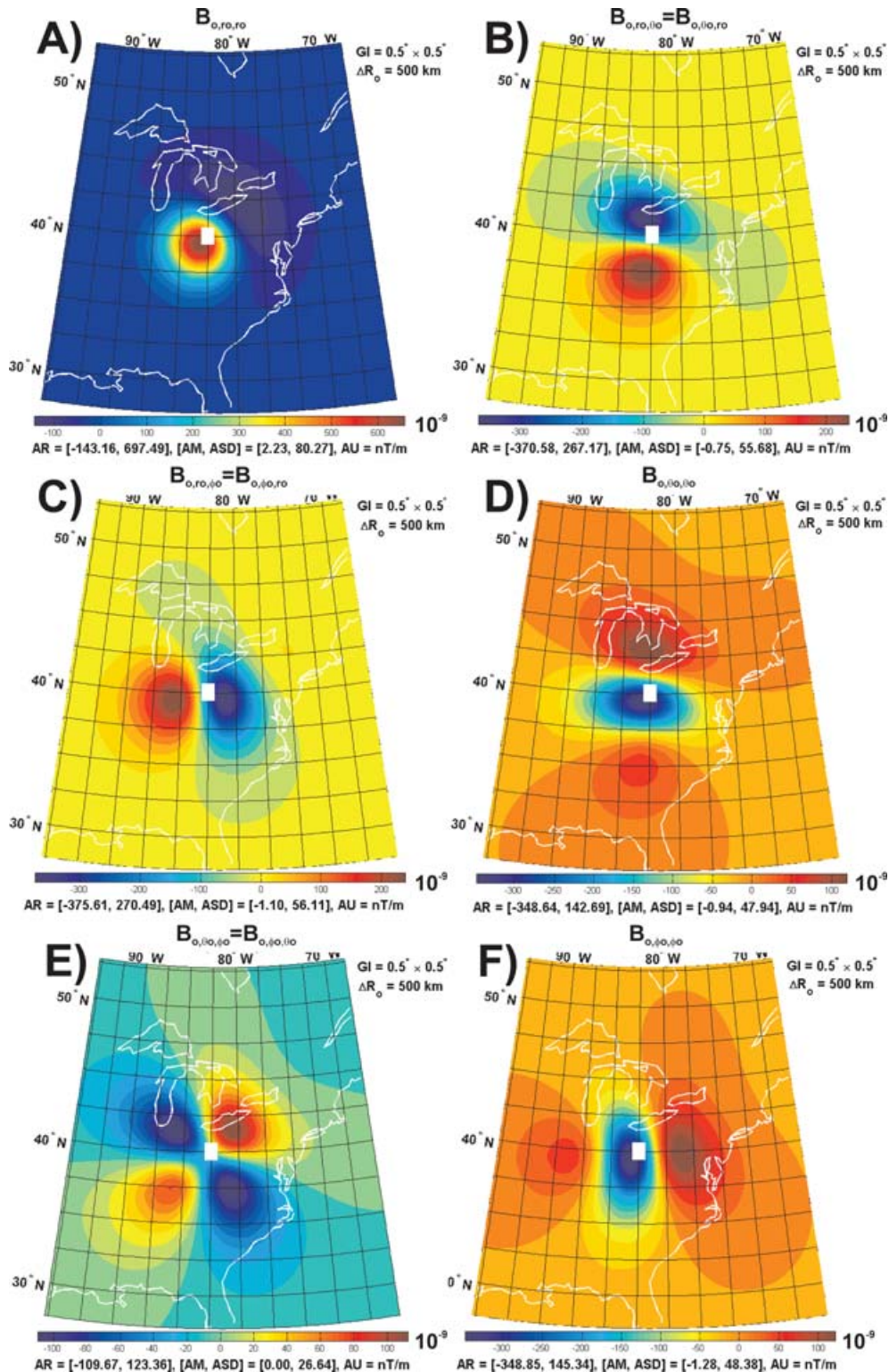


Figure 7. Magnetic tensor gradient components in the Observation-centred coordinate system for the spherical prism in Fig. 6.

3 CRUSTAL PRISM MAGNETIC EFFECTS

The polarities of the above magnetic effects of the simple spherical prism vary depending on the interpretational perspective from which the problem is being considered. For example, in deriving the results in the previous section, we adopted the Earth-centred spherical coordinate convention where the positive unit vectors in the r_o -, θ_o - and ϕ_o - directions, respectively, point outward from the Earth's centre, southward from the North Pole, and eastward from zero longitude (Fig. 3). However, geophysical practice follows the Observation-centred convention where the positive unit vectors in the r_o -, θ_o - and ϕ_o - directions are, respectively, downward, northward and eastward of the observation station located on or above the Earth's surface (e.g. Blakely 2001). Thus, to transform to the Observation-centred convention, we reverse the polarities of the geocentric expressions for B_{o,r_o} (eq. 22a), B_{o,θ_o} (eq. 22b), and the tensor elements of $B_{o,r_o,\phi_o} = B_{o,\phi_o,r_o}$ and $B_{o,\theta_o,\phi_o} = B_{o,\phi_o,\theta_o}$ (Matrix 23).

To facilitate the use of our analytical expressions, we give in Figs 4–9 the Observation-centred spherical coordinate magnetic effects at the altitude of 500 km for a $1^\circ \times 1^\circ \times 10$ km prism centred on Ohio with its top surface at sea level. The prism is magnetized with an intensity of 1 Am^{-1} and $D_s = I_s = 0^\circ$ (Figs 4 and 5), $D_s = I_s = 45^\circ$ (Figs 6 and 7) and $D_s = I_s = 90^\circ$ (Figs 8 and 9). These effects were modelled for the prism by GLQ integration using 128 nodes with 8 nodes spanning each of the two horizontal dimensions and 2 nodes spanning the vertical dimension of the prism's volume.

Maps A–D of Figs 4, 6 and 8, respectively, show the prism's magnetic potential and field vector r_o -, θ_o - and ϕ_o -components modelled from the GLQ integration of eqs (21), (22a), (22b) and (22c), respectively. In Figs 5, 7 and 9, Maps A–F show the magnetic gradient tensor components from the GLQ integration of the three trace and three unique off-diagonal elements of the symmetric Matrix 23. Note that four of the nine elements are redundant because $B_{o,r_o,r_o} = B_{o,\theta_o,r_o}$, $B_{o,r_o,\phi_o} = B_{o,\phi_o,r_o}$ and $B_{o,\theta_o,\phi_o} = B_{o,\phi_o,\theta_o}$, and Laplace's equation relates any two components of B_{o,r_o,r_o} , B_{o,θ_o,θ_o} and B_{o,ϕ_o,ϕ_o} to the third one.

Fig. 10 shows the effects of induced magnetization with inclinations and declinations taken from the IGRF updated to 2006 January 1. The induced magnetization intensities were estimated by multiplying the IGRF intensities (Map A) with 0.01 SI volume magnetic susceptibility that was assumed for the prism. Maps B–D give the B_{o,r_o} , B_{o,θ_o} and B_{o,ϕ_o} components, respectively, at 500 km altitude for the induced magnetization of the prism. Map E shows the anomalous magnetic field obtained from $B_{o,T} = (B_{o,r_o}^2 + B_{o,\theta_o}^2 + B_{o,\phi_o}^2)^{1/2}$, whereas Map F

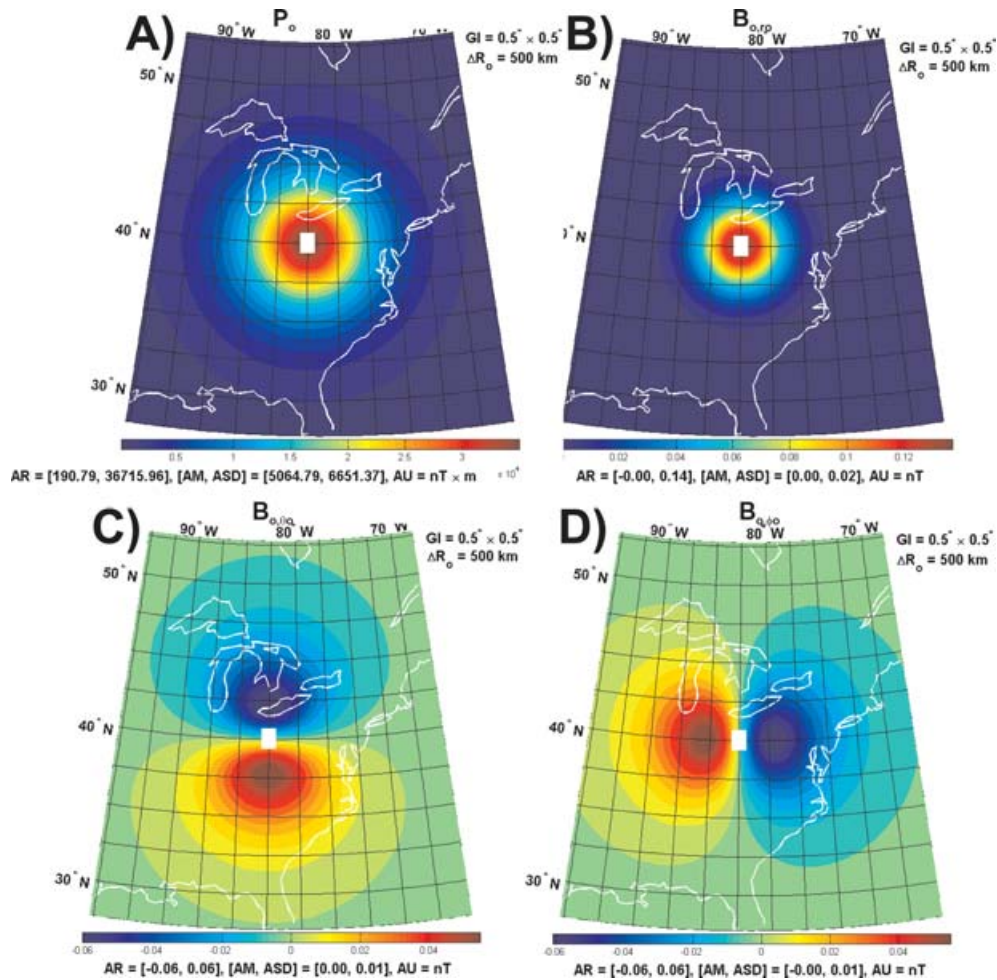


Figure 8. Maps A–D give the respective magnetic potential (P_o) and magnetic radial (B_{o,r_o}), north–south (B_{o,θ_o}) and east–west (B_{o,ϕ_o}) vector anomaly components in the Observation-centred coordinate system for the spherical prism in Fig. 4 with $D_s = I_s = 90^\circ$.

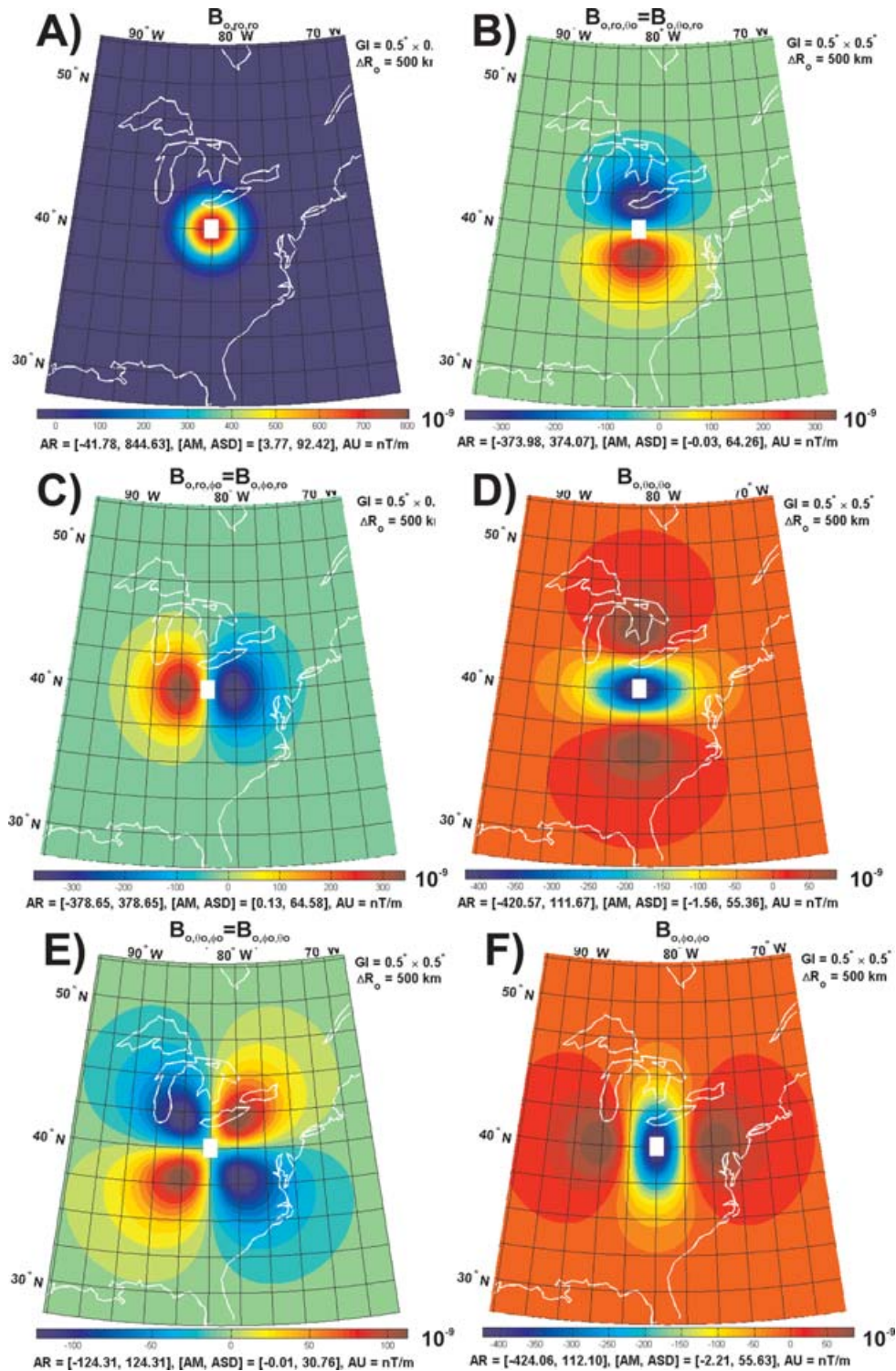


Figure 9. Magnetic tensor gradient components in the Observation-centred coordinate system for the spherical prism in Fig. 8.

gives the corresponding total field anomaly ($B_{o,T} - B_{IGRF}$), where B_{IGRF} is the IGRF field intensity at 500 km altitude. The total field anomaly facilitates comparing satellite magnetic observations with airborne, ship, and other near-surface surveys that, in general, map scalar total anomaly intensities without measuring the vector components (e.g. von Frese *et al.* 1981a,b; von Frese 1998; Blakely 2001).

4 SATELLITE ALTITUDE CRUSTAL MAGNETIC EFFECTS OF THE MIDDLE EAST

As another example, we demonstrate the use of the formulae obtained in Section 3 above to process magnetic data on a spherical patch of the Earth. Global spherical harmonic geomagnetic field models are limited in representing lithospheric anomalies because they typically do not

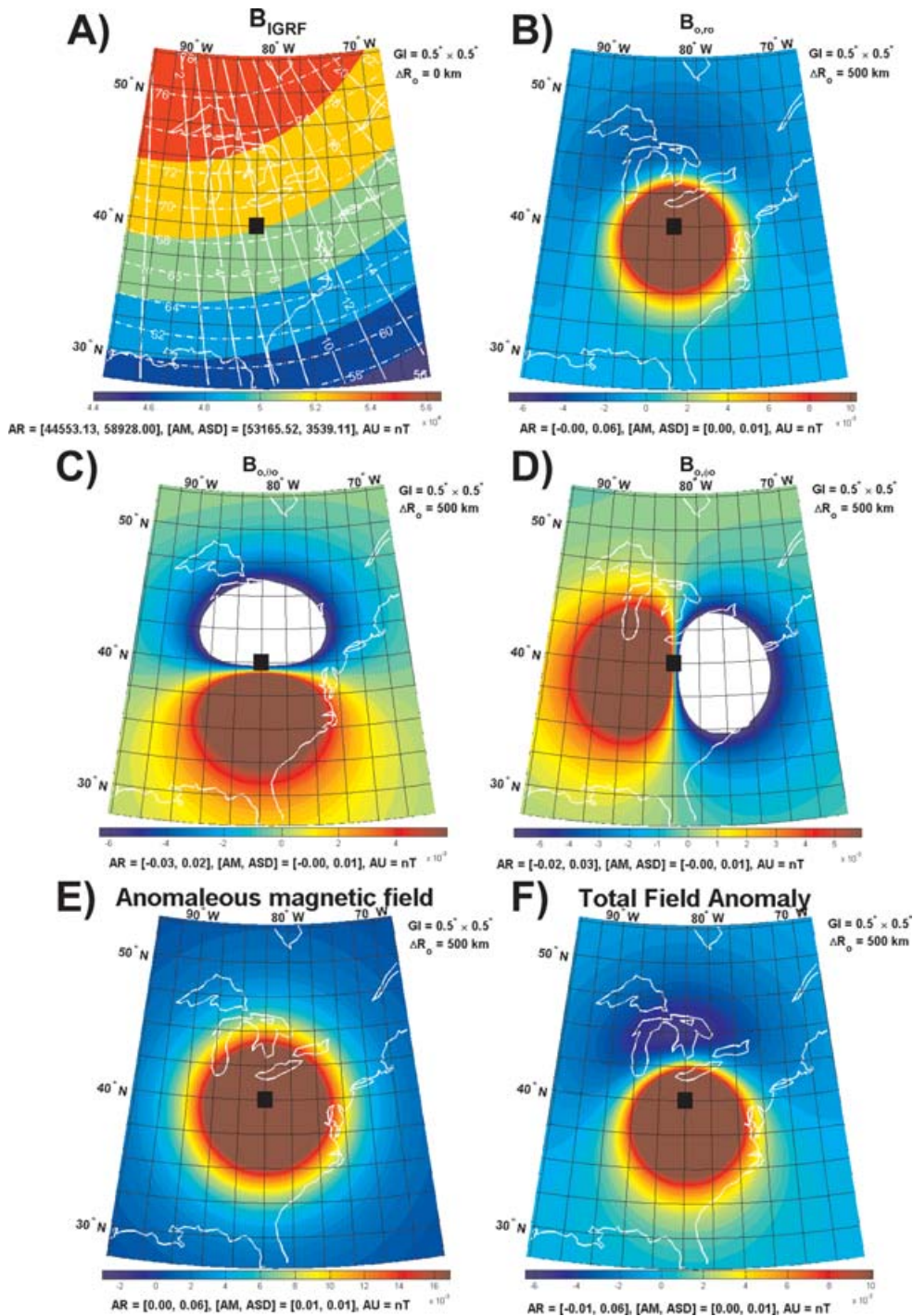


Figure 10. Induced magnetization effects for a prism with a volume susceptibility of 0.01 SI under the polarizing effects of the IGRF 2006 updated to January 1st 2006. Map A gives the IGRF's intensity (colour), inclination (dashed white contours), and declination (solid white contours) variations.

incorporate local geological constraints on these anomaly components. However, geological constraints over finite spherical patches can be applied to crossing satellite orbital data tracks to extract local lithospheric anomalies with much improved accuracies and details relative to the primitive data averages that spherical harmonic models commonly take for the anomaly estimates (e.g. von Frese & Kim 2003; Kim *et al.* 2007).

In general, the more effective approach in extracting and interpreting lithospheric anomalies over the spherical patch is to represent the anomalies by the magnetic effects of an equivalent point source (EPS) distribution (von Frese *et al.* 1981b, 1988; von Frese 1998). Least-squares matrix inversion relates the spherical patch magnetic anomalies to the magnetic moments of a fixed distribution of magnetic point dipoles. The derived EPS model, in turn, can be evaluated for least-squares estimates of any analytical attribute of the magnetic anomalies (e.g. their potential and spatial derivatives, vertical and horizontal continuations, etc.).

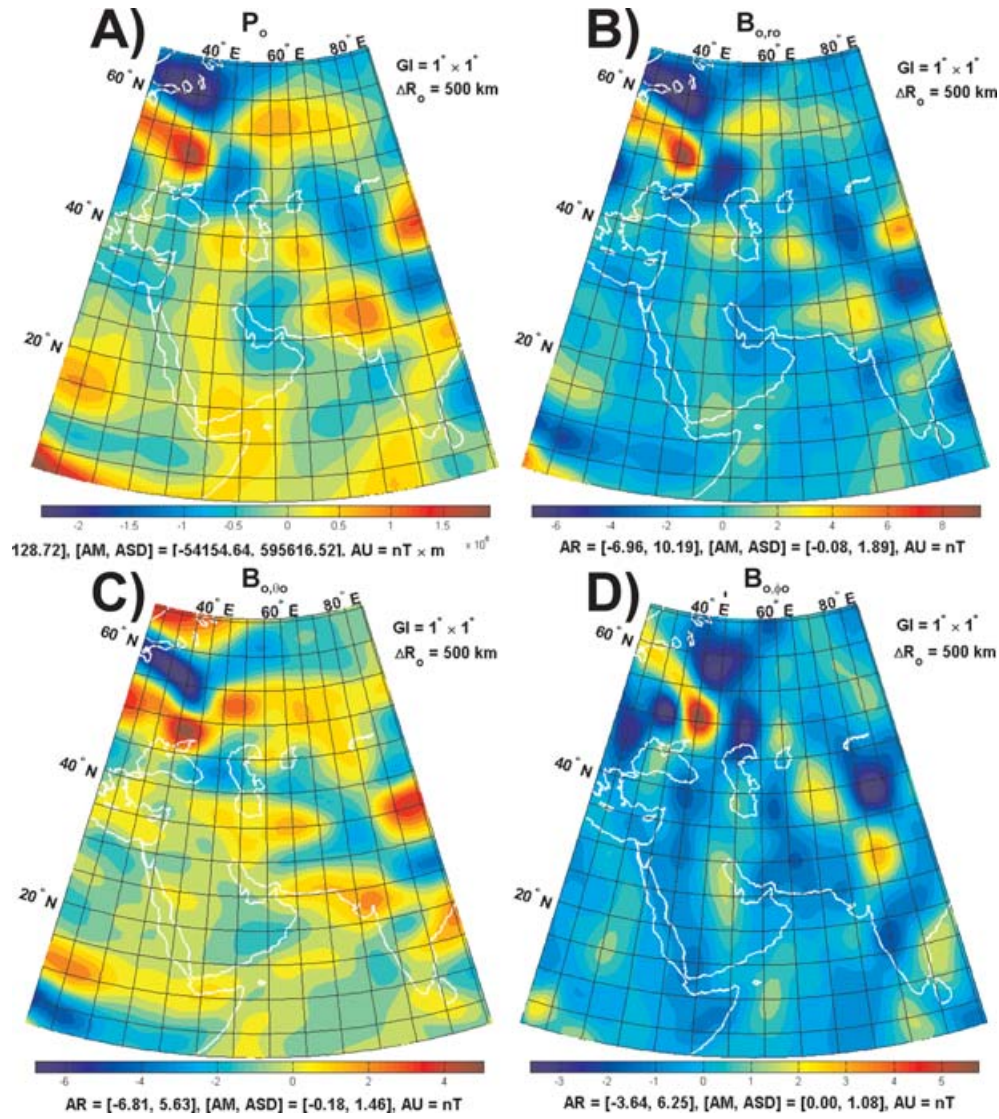


Figure 11. Maps A–D show in the Observation-centred coordinate system the magnetic potential (P_o), and the vector magnetic radial (B_{o,r_o}), north-south (B_{o,θ_o}) and east-west (B_{o,ϕ_o}) components of the CHAMP data for the Middle East.

Over the large area of the Middle East centred on Iran, for example, we modelled the radial crustal anomalies of the CHAMP satellite magnetic observations by EPS inversion to evaluate the lithospheric vector and tensor gradient components shown in Figs 11 and 12, respectively. Here, we evaluated the radial crustal magnetic (B_{o,r_o})-estimates from the 16–90 degree and order spherical harmonic components of the CHAMP MF4 model (Maus *et al.* 2006). These 65×65 estimates were obtained at 500 km altitude over the $1^\circ \times 1^\circ$ grid covering 1°N – 65°N latitudes and 22°E – 86°E longitudes and related to the radial magnetic effects of the underlying $2^\circ \times 2^\circ$ distribution of 33×33 equivalent point dipoles by least-square matrix inversion.

The inversion assumed negligible crustal magnetic remanence so that the CHAMP radial component observations were modelled by the induced magnetism form of eq. 22(a) as:

$$dB_{o,r_o} = -\frac{\mu_o}{4\pi} \frac{1}{R_{os}^5} [(H_{s,x} \sin \theta_o \cos \phi_o + H_{s,y} \sin \theta_o \sin \phi_o + H_{s,z} \cos \theta_o) R_{os}^2 - 3(r_o - r_s \cos \delta)(H_{s,x} R_{os,x} + H_{s,y} R_{os,y} + H_{s,z} R_{os,z})] d\chi_s. \quad (28)$$

The scalar $d\chi_s$ is the isotropic magnetic susceptibility that when multiplied, for example, against the geomagnetic field intensity component $H_{s,x}$ from the appropriately updated IGRF gives the x -component intensity of the dipole's induced magnetic moment. eq. (28) describes the system of linear equations that relates the CHAMP radial component observations B_{o,r_o} to the assumed distribution of point dipoles by the unknown set of magnetic susceptibilities χ_s . By least-squares matrix inversion, we obtained susceptibilities of the point dipoles with the radial component effects in Fig. 11(B) that matched CHAMP MF4 estimates with negligible error. In addition, the EPS model estimated

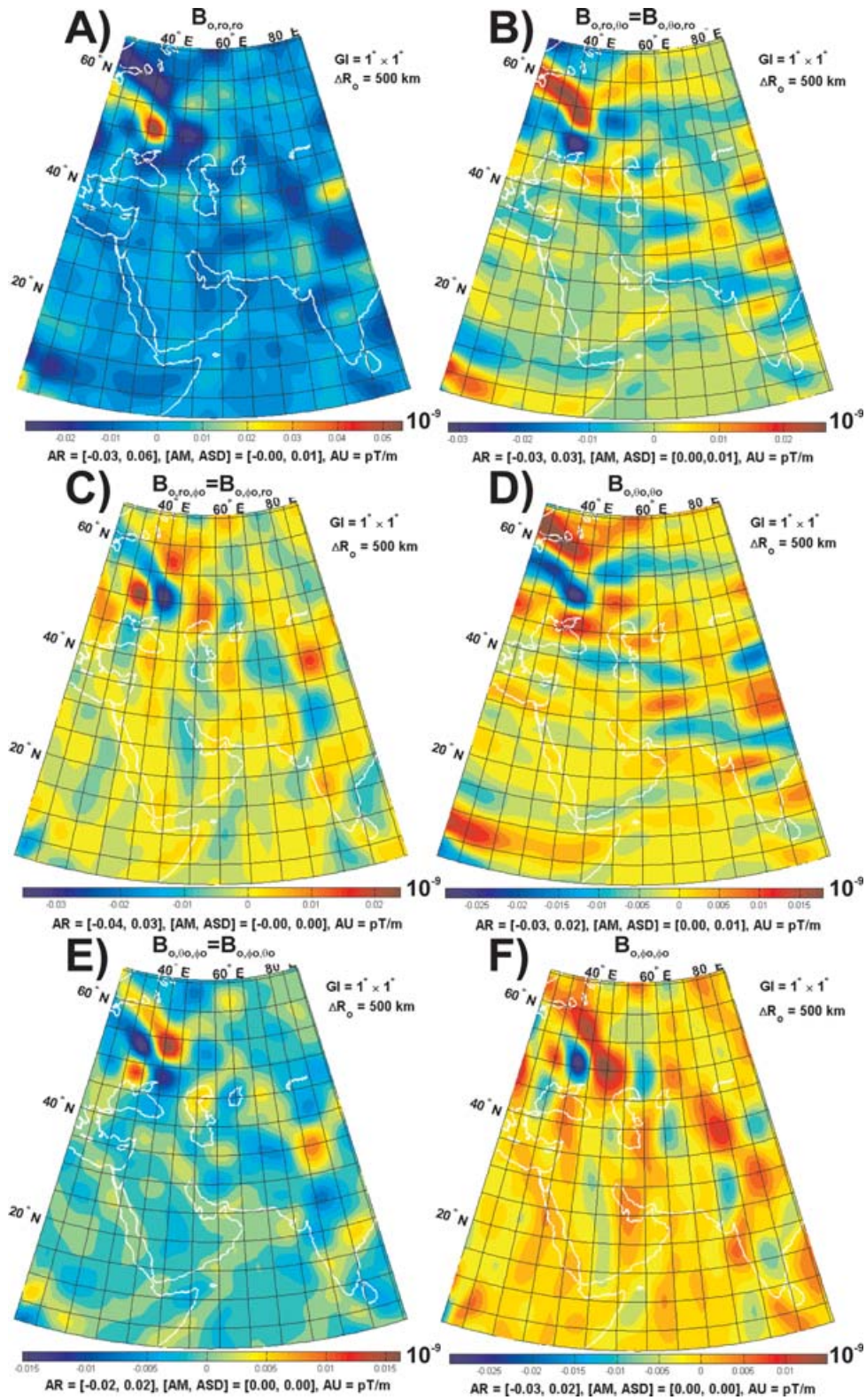


Figure 12. Maps A–F show in the Observation-centred coordinate system the magnetic tensor gradient components of the CHAMP data for the Middle East.

with negligible error the other two vector components in Figs 11(C) and (D), the magnetic potential in Fig. 11(A), and the magnetic tensor gradients in Fig. 12.

The inducing geomagnetic field variations over the EPS array shown in Fig. 13(C) substantially distort the spatial relationships between the CHAMP anomalies and their lithospheric sources (von Frese *et al.* 1981b, 1982, 1997; von Frese 1998). These variations cause the lithospheric sources to have much stronger and more source-centred effects in the northern study region than in the southern portion where

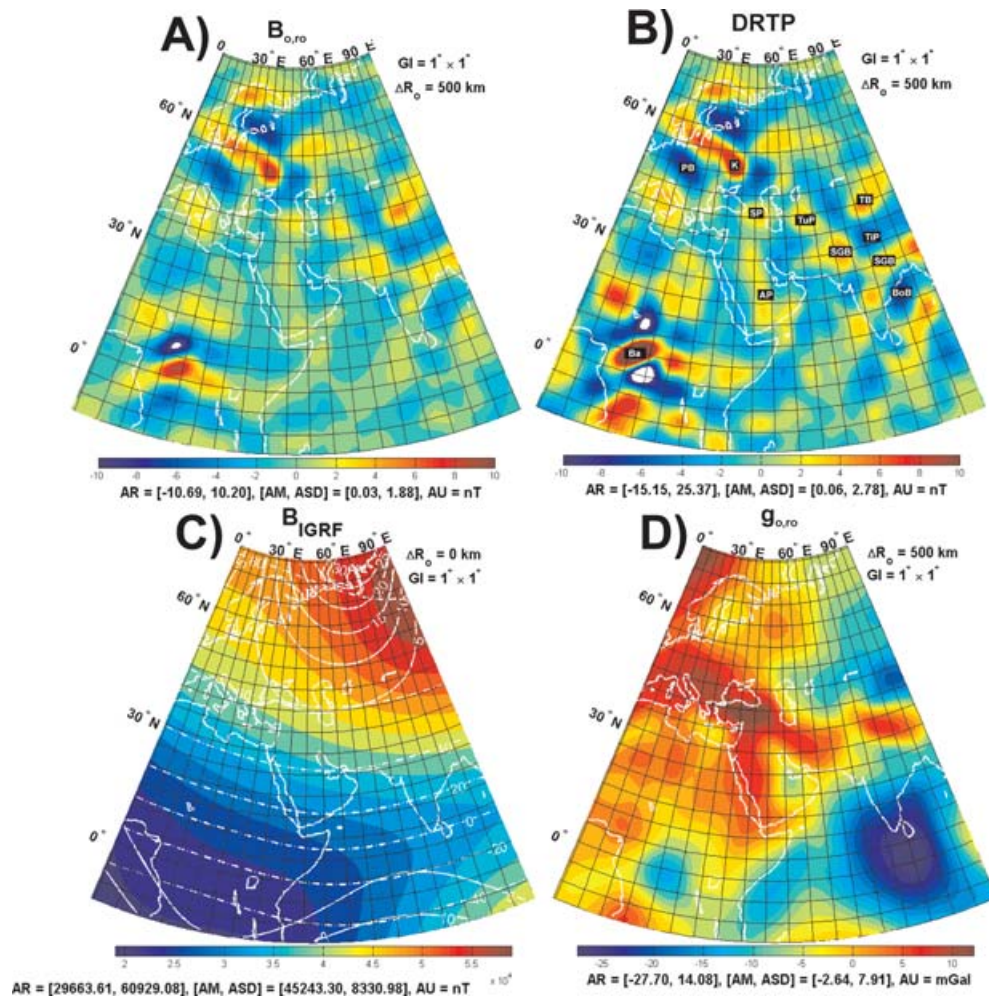


Figure 13. CHAMP crustal radial magnetic components $B_{o,ro}$ in Map A are differentially reduced to the pole (DRTP) in Map B for the polarizing core field effects of the IGRF updated to January 1st 2006. Map C illustrates the IGRF's intensity (colour), inclination (dashed white contours), and declination (solid white contours) variations. Comparing the DRTP anomalies with the GRACE gravity anomalies in Map D facilitates identifying magnetic anomaly sources that also may constitute density contrasts of the crust, especially where crustal magnetic remanence is negligible. Map D gives the gravity anomalies of the region mapped by the GRACE satellite mission.

geomagnetic field intensities and inclinations are much lower. To express the anomalies more directly in terms of the magnetic susceptibility variations of the lithosphere, we can differentially reduce them to what they would be at the geomagnetic pole (von Frese *et al.* 1981b; von Frese 1998).

Fig. 13(B), for example, gives the differentially reduced-to-pole (DRTP) estimates for the radial component anomalies of Fig. 13(A) that we obtained from evaluating the EPS model with the uniform geomagnetic field of intensity $H_s = 60\,000$ nT, inclination $I_s = 90^\circ$, and declination $D_s = 0^\circ$. In Fig. 13, we extended the source and observation grids to bring out better the contrast between the higher latitude and equatorial anomalies. Thus, the source grid was extended to 46×48 nodes at $2^\circ \times 2^\circ$ spacing, and the observation grid to 91×96 nodes at $1^\circ \times 1^\circ$ spacing, with the SW corners of both grids starting at $(0^\circ E, 15^\circ S)$.

Assuming magnetic remanence is negligible, the DRTP anomalies are now centred on their lithospheric sources with amplitude variations that directly reflect magnetic susceptibility variations of the lithosphere. Comparison of Maps A and B shows that the DRTP adjustment only mildly affected the higher latitude anomalies over the Scythian Platform (SP), Turan Plate (TuP), Kursk (K), Tibet Plateau (TiP), plus the Panonnian (PB), Sindhu Ganga (SGB) and Tarim (TB) Basins, whereas in the lower latitudes over westcentral Africa, the Arabian Plate (AP) and the Bay of Bengal (BoB), more substantial adjustments of the anomaly amplitudes and spatial details are evident. The DRTP anomalies clearly suggest that the most strongly magnetized lithosphere of the study area is in westcentral Africa and the Kursk region of Russia. The westcentral African region is overlain by the Bangui magnetic anomaly (Ba) related perhaps to intrusions of uplifted crust from a meteorite impact (Girdler *et al.* 1992), whereas the Kursk anomaly appears to signal the effects of anomalously thickened crust (Taylor & Frawley 1987).

Of course, these results, like those of any magnetic analysis, are not unique because of the source ambiguity of magnetic anomalies. Thus, to help resolve interpretational ambiguities, additional geological and geophysical constraints are necessary. Here, the DRTP anomalies

are especially well suited for comparing with gravity anomalies (e.g. Map D) and other source-centred data sets like geological, photographic, heat flow and seismic observations.

5 CONCLUSIONS

GLQ integration yields accurate and efficient numerical modelling of the spherical prism's magnetic potential, vector and tensor gradient components for quantitative spherical coordinate studies of regionally magnetized bodies. Effective magnetic modelling accuracy is achieved by using a sufficient number of nodes so that the distance to the observation point is greater than the node spacing. However, further modelling accuracy is always possible by increasing the number of point nodes in a prism or subdividing the prism into a set of smaller prisms. These approaches can also be used to accommodate magnetization variations within a prism. Furthermore, accurate magnetic modelling on the surface of the prism is possible because the nodes are displaced away from the surface into the interior of the prism. Thus, the lack of modelling singularities at the prism's surface allows our procedures to compute accurate magnetic effects of the spherical prism anywhere on or above its surface. These results facilitate geological studies of the spherical coordinate magnetic observations of the Earth and other planets that are becoming increasingly available.

ACKNOWLEDGMENTS

We thank the anonymous reviewers for their constructive comments on this manuscript. The US National Science Foundation under grant NSF-OPP 0338005, the Ohio Supercomputer Center and the School of Earth Sciences at The Ohio State University, and Shell Oil Company supported elements of this research.

REFERENCES

- Anderson, J.C., 1922. *Magnetism and Magnetic Materials*, Chapman & Hall, London.
- Arkani-Hamed, J., 2004. A coherent model of the crustal magnetic field of Mars, *J. geophys. Res.*, **109**, 1–8.
- Barritt, S.D., 1993. The African Magnetic Mapping Project (AMMP), *ITC J.*, **2**, 122–131.
- Blakely, R.J., 2001. *Potential Theory in Gravity & Magnetic Applications*, Cambridge University Press, Cambridge.
- Busby, J.P., Peart, R.J., Green, C.A., Ogilvy, R.D. & Williamson, J.P., 1991. A search for direct hydrocarbon indicators in the Formby area, *Geophys. Prospect.*, **39**(5), 691–710.
- ESA, 2004. Swarm-The Earth's Magnetic Field and Environmental Explorers, in *ESA Publ. Div., ESA SP-1279(6), ESTEC*, Noordwijk, NL, p. 61.
- Finn, C.A., Pilkington, M., Cuevas, A., Hernandez, I. & Urrutia, J., 2001. New digital magnetic anomaly database for North America, *The Leading Edge*, **20**(8), 870–872.
- Girdler, R.W., Taylor, P.T. & Frawley, J.J., 1992. A possible impact origin for the Bangui magnetic anomaly (Central Africa), *Tectonophysics*, **212**(1), 45–58.
- Golynsky, A.V. et al., 2001. *ADMAP-Magnetic Anomaly Map of the Antarctic*. BAS (Misc) 10, 1:10000000 Scale Map, Cambridge, British Antarctic Survey.
- Hemant, K., Thébault, E., Manda, M., Ravat, T. & Maus, S., 2007. Magnetic Anomaly map of the World: merging satellite, airborne, marine and ground-based magnetic data sets, *Earth planet. Sci. Lett.*, **260**(1), 56–71.
- Hinze, W.J., Hood, P.J. & the, Committee for the Magnetic Anomaly Map of North America, 1988. Magnetic Anomaly map of North America, *The Leading Edge*, **7**(11), 19–21.
- Kim, H.R., von Frese, R.R.B., Taylor, P.T., Golynsky, A.V. & Gaya-Piqué, L.R., 2007. Improved magnetic anomalies of the Antarctic lithosphere from satellite and near-surface data, *Geophys. J. Int.*, **171**(46), 119–126.
- Ku, C.C., 1977. A direct computation of gravity and magnetic anomalies caused by 2- and 3-dimensional bodies of arbitrary shape and arbitrary magnetic polarization by equivalent point method and a simplified cubic spline, *Geophysics*, **42**(3), 610–622.
- Langel, R.A. & Hinze, W.J., 1998. *The Magnetic Field of the Earth's Lithosphere (The Satellite Perspective)*, Cambridge University Press, Cambridge.
- Lin, R.P. et al., 1998. Lunar surface magnetic fields and their interaction with the solar wind: results from Lunar Prospector, *Science*, **281**(5382), 1480–1484.
- Maus, S., Rother, M., Hemant, K., Stolle, C., Lühr, H. & Kuvshinov, A., 2006. Earth's lithospheric magnetic field determined to spherical harmonic degree 90 from CHAMP satellite measurements, *Geophys. J. Int.*, **164**(17), 319–330.
- Merayo, J.M.G., Brauer, P., Primdahl, F., Petersen, J.R. & Nielsen, O.V., 2000. Scalar calibration of vector magnetometers, *Measur. Sci. Technol.*, **11**, 120–132.
- Mushayandebvu, M.F. & Davies, J., 2006. Magnetic gradients in sedimentary basins: examples from the Western Canada Sedimentary Basin, *The Leading Edge*, **25**(1), 69–73.
- Pereira, R.P. & Fuck, R.A., 2005. Archean nucleii and the distribution of kimberlite and related rocks in the Sao Francisco craton, Brazil, *Revista Brasileira de Geociencias*, **35**(3), 93–104.
- Reeves, C.V., 2001. The role of airborne geophysical reconnaissance in exploration geoscience, *First Break*, **19**(9), 501–508.
- Reeves, C.V., 2003. AAIME (Aeromagnetism of Arabia, India and the Middle East), CD-ROM version, ITC.
- Sharma, P.V., 1986. *Geophysical Methods in Geology*, Elsevier, Amsterdam.
- Sjogren, W.L. et al., 1997. The Venus gravity field and other geodetic parameters, in *Venus II: Geology, Geophysics, Atmosphere, and Solar Wind Environment*, Vol. 284, pp. 1125–1161, eds Bougher, S.W., Hunten, D.M. & Phillips, R.J., University of Arizona Press, Tucson, AZ.
- Stroud, A.H. & Secrest, D., 1966. *Gaussian Quadrature Formulas*, Prentice-Hall, New Jersey.
- Taylor, P.T. & Frawley, J.J., 1987. Magsat anomaly data over the Kursk region, U.S.S.R., *Phys. Earth Planet. Inter.*, **45**(3), 255–265.
- Verhoef, J.R., Macnab, R., Roest, W. & Arkani-Hamed, J., 1996. *Magnetic anomalies of the Arctic and North Atlantic oceans and adjacent land areas*, Open file 3125a, Geological Society of Canada.
- von Frese, R.R.B., 1998. Correction to: R.R.B. von Frese, W.J. Hinze, L.W. Braile, 'Spherical Earth gravity and magnetic anomaly analysis by equivalent point source inversion Earth Planet. Sci. Lett. 53 (1981) 69–83', *Earth planet. Sci. Lett.*, **163**(1), 409–411.
- von Frese, R.R.B. & Kim, H.R., 2003. Satellite magnetic anomalies for lithospheric exploration, in *OIST-4 Proceedings (4th Ørsted International Science Team Conference)*, pp. 115–118, eds Stauning, P., Lühr, H., Ultré-Guérard, P., LaBrecque, J., Purucker, M., Primdahl, F., Jørgensen, J.L., Christiansen, F., Høeg, P. & Lauritsen, K.B., Narayana Press, Copenhagen.

- von Frese, R.R.B., Hinze, W.J. & Braile, L.W., 1982. Regional North American gravity and magnetic anomaly correlations, *Geophys. J. R. astr. Soc.*, **69**, 745–761.
- von Frese, R.R.B., Ravat, D.N. & Hinze, W.J., 1988. Improved inversion of geopotential field anomalies for lithospheric investigations, *Geophysics*, **53**(3), 375–385.
- von Frese, R.R.B., Jones, M.B., Kim, J.W. & Li, W.S., 1997. Spectral correlation of magnetic and gravity anomalies of Ohio, *Geophysics*, **62**(1), 365–380.
- von Frese, R.R.B., Hinze, W.J., Braile, L.W. & Luca, A.J., 1981a. Spherical earth gravity and magnetic anomaly modelling by Gauss–Legendre quadrature integration, *J. Geophys.*, **49**(3), 234–242.
- von Frese, R.R.B., Hinze, W.J. & Braile, L.W., 1981b. Spherical earth gravity and magnetic anomaly analysis by equivalent point source inversion, *Earth planet. Sci. Lett.*, **53**(1), 69–83.
- Wonik, T., Trippler, K., Geipel, H., Greinwald, S. & Pashkevitch, I., 2001. Magnetic Anomaly map for Northern, Western and Eastern Europe, *Terra Nova*, **13**(3), 203–213.